scientific reports

Check for updates

OPEN

A deep learning-based computed tomography reading system for the diagnosis of lung cancer associated with cystic airspaces

Zeyang Hu[2], Xia Zhang[3], Jinqiu Yang[3], Bailing Zhang[3], Hang Chen[1], Wei Shen[2], Hongxiang Li[1], Yipeng Zhou[3], Jiaheng Zhang[1], Keyue Qiu[1], Zijun Xie[1], Guodong Xu[1]✉, Jian Tan[3]✉ & Chaoyi Pang[3]✉

To propose a deep learning model and explore its performance in the auxiliary diagnosis of lung cancer associated with cystic airspaces (LCCA) in computed tomography (CT) images. This study is a retrospective analysis that incorporated a total of 342 CT series, comprising 272 series from patients diagnosed with LCCA and 70 series from patients with pulmonary bulla. A deep learning model named LungSSFNet, developed based on nnUnet, was utilized for image recognition and segmentation by experienced thoracic surgeons. The dataset was divided into a training set (245 series), a validation set (62 series), and a test set (35 series). The performance of LungSSFNet was compared with other models such as UNet, M2Snet, TANet, MADGNet, and nnUnet to evaluate its effectiveness in recognizing and segmenting LCCA and pulmonary bulla. LungSSFNet achieved an intersection over union of 81.05% and a Dice similarity coefficient of 75.15% for LCCA, and 93.03% and 92.04% for pulmonary bulla, respectively. These outcomes demonstrate that LungSSFNet outperformed many existing models in segmentation tasks. Additionally, it attained an accuracy of 96.77%, a precision of 100%, and a sensitivity of 96.15%. LungSSFNet, a new deep-learning model, substantially improved the diagnosis of early-stage LCCA and is potentially valuable for auxiliary clinical decision-making. Our LungSSFNet code is available at https://github.com/zx0412/LungSSFNet.

Keywords Computed tomography (CT), Convolutional neural network, Deep learning, Pulmonary nodule, LCCA

Lung cancer is one of the most common malignant tumors worldwide, and its early diagnosis and treatment remain major challenges[1,2]. Screening for early-stage lung cancer is usually performed using low-dose chest computed tomography (CT)[3], which reveals various forms of nodules, including ground-glass nodules, mixed-density nodules, and solid nodules[4]. In contrast, a rare type of lung cancer known as lung cancer associated with cystic airspaces (LCCA) primarily appears in CT images as a thin-walled cystic cavity with or without solid or ground-glass nodules[5,6]. LCCA accounts for approximately 3.7% of lung cancers diagnosed in initial CT examinations[7]. The characteristic imaging features of LCCA have resulted in cases of LCCA being reported in different ways, such as carcinoma of the bronchus presenting as thin-walled cysts[8], carcinoma masquerading as a thin walled cyst[9], bronchogenic carcinoma and giant bullous disease[10], bronchioloalveolar carcinoma arising in longstanding lung cysts[11], and lung carcinoma associated with bullous lung disease[12]. Moreover, due to the difficulty in differentiating the CT features of LCCA from those of benign diseases, such as lung pustules, and the difficulty of puncture biopsy, LCCA can be misdiagnosed, ultimately resulting in the transformation of early-stage disease into advanced-stage or metastatic disease. There are four possible mechanisms for the development of LCCA[13]: (1) obstruction of the gas outflow pathway due to formation of a one-way valve-type structure in the small airways; (2) adherent growth of tumor cells covering a damaged alveolar wall; (3) formation of a cystic tumor; and (4) growth of a tumor along the wall of the pre-existing lung plexus. It is generally believed that mechanism (1) is the main cause of LCCA, i.e., a growing tumor compresses the small airways and thereby forms a structure similar to a one-way valve. As a result, gas can easily enter the small airways but has difficulty exiting,

[1]Ningbo Medical Center Lihuili Hospital, Ningbo, China. [2]The Third People's Hospital Health Care Group Of Cixi, Ningbo, China. [3]NingboTech University, Ningbo, China. ✉email: xuguodong@nbu.edu.cn; jt@nit.zju.edu.cn; chaoyi.pang@qq.com

leading to an abnormal expansion of the distal alveolar spaces. This enlargement appears as cystic-cavity-like features in imaging.

The atypicality of the imaging features of LCCA means that it is highly challenging for radiologists and thoracic surgeons to diagnose[14,15]. Therefore, we recognized that an artificial intelligence (AI) system may be useful for the identification of chest CTs containing possible features of LCCA, thereby reducing the workload of doctors while minimizing the rates of misdiagnosis and delayed diagnosis[16,17]. With the development of AI technique and the enhancement of computing power, a large number of deep learning techniques have been successfully applied to image processing[18]. Ronneberger et al.[19] first suggested uing U-Net for biomedical image segmentation and proposed a model that was widely applied for the analysis of medical images, especially for the detection of lung nodules. Subsequently, UNet+[20] was developed, due to continuous updating and iteration of deep learning[21,22], to generate even better models for the refinement of imaging recognition[18,23]. To reduce false negatives, Sun et al. constructed a new model by measuring nodule size, type, and location to enable the effective preoperative assessment of patients with lung adenocarcinoma[24].

Following the great success of using deep learning techniques for segmenting images[25], a new deep convolutional neural network developed by Men et al. was used to generate a model for automatic segmentation of rectal cancer during radiotherapy[26]. Similarly, Wang et al. proposed a model that is almost comparable to manual segmentation in its ability to segment nasopharyngeal cancer[27,28]. Therefore, combining a nodule recognition function with the segmentation function of a deep learning model may enable the identification and delineation of possible malignancy areas in chest CT images, thereby improving the reading efficiency of imaging physicians.

In this study, we used a deep learning technique to construct a model to realize the effective diagnosis of LCCA. Specifically, we constructed a model based on a novel attention module called the multi-frequency in multi-scale SimAM attention (SSF) block, and thus named the model LungSSFNet. Unlike a traditional U-Net-type model, LungSSFNet integrates shallow features and deep semantic features. In addition, it combines the frequency domain, spatial domain, and a SimAM model based on multi-scale features. Moreover, LungSSFNet formulates weight generation as an energy function and derives its closed-form solution to obtain three-dimensional, parameter-free attention weights.

In experimental tests, LungSSFNet outperformed all tested imaging models in terms of precision and accuracy, indicating that it can be applied in clinical settings.

Materials and methods

To achieve good performance in the segmentation of LCCA, LungSSFNet integrates a multi-scale and multi-frequency module constructed on the basis of nnUNet. As shown in Fig. 1, this module fuses shallow features with deep semantic features and is denoted as SSF.

Semantic features are used to distinguish benign and malignant features as judged by human readers and can be influenced by visual morphological features. In this study, these features included nodule-specific features, such as tumor components, lesion morphology, contrasting edge structures, and internal features.

Fusion of shallow features and deep semantic features

As depicted in Fig. 1, deep semantic features and shallow features are denoted as X_{DF} and X_{SF}, respectively. LungSSF adopts nnUnet as its basic network structure in which each CONV2D layer is composed of two 3 × 3 convolutions with a stride of 1, and each $block_i$ (i = 1, ……, 10) is composed of two 3 × 3 convolutions with a stride of i. After passing through the convolution layer to $block_{10}$, X_{DF} are formed. Each convolution layer has two learnable parameters, α and β. Thus, Y_i is formed by the operation of two operators, S and U, where S stands for subtraction unit and U stands for feature splicing, as follows:

$$Y_i = \alpha_i \times \mathrm{Conv}(X_i) + \beta_i \times \mathrm{Conv}(|X_{DF_i} \ominus X_{SF_i}|)$$

$$X_i = \mathrm{Cat}(\mathrm{Up}(\mathrm{SimAM}(X_{DF_i})), X_{SF_i})$$

where Cat (·) is a two-dimensional (2D) convolution with a core size of 3; Up (·) is interpolation; SimAM(·) is parameter-free attention; ⊖ is the element-wise subtraction operation, |·| calculates the absolute value, and Conv(·) is a 2D convolution with a kernel size of 3.

The abovementioned operations highlight the contours in an image and assist the model in capturing important details of the image.

Multi-frequency in multi-scale SimAM attention

Humans acquire visual information at multiple scales, allowing that human experts can analyze medical images in substantially different ways. Thus, three-dimensional weight must be formed by defining the energy functions of neurons. Subsequently, these functions are combined with frequency and spatial domain information to generate a multi-scale SimAM attention weight, which is defined as multi-frequency in the SSF module.

Based on the property of linear inhibition of neurons, an energy function of neurons can be defined as follows:

$$e_t(\omega_t, b_t, \mathbf{y}, x_i) = (y_t - \hat{t})^2 + \frac{1}{M-1}\sum_{i=1}^{M-1}(y_i - \hat{x}_i)^2 + \lambda\,\omega_t^2$$

where the target neuron is $\hat{t} = \omega_t t + b_t$ and the other neurons are $\hat{x}_i = \omega_t x_i + b_t$, which are the elements of the input feature map $X \in R^{C*H*W}$ in a single channel. The optimization of ω_t and b_t is performed using

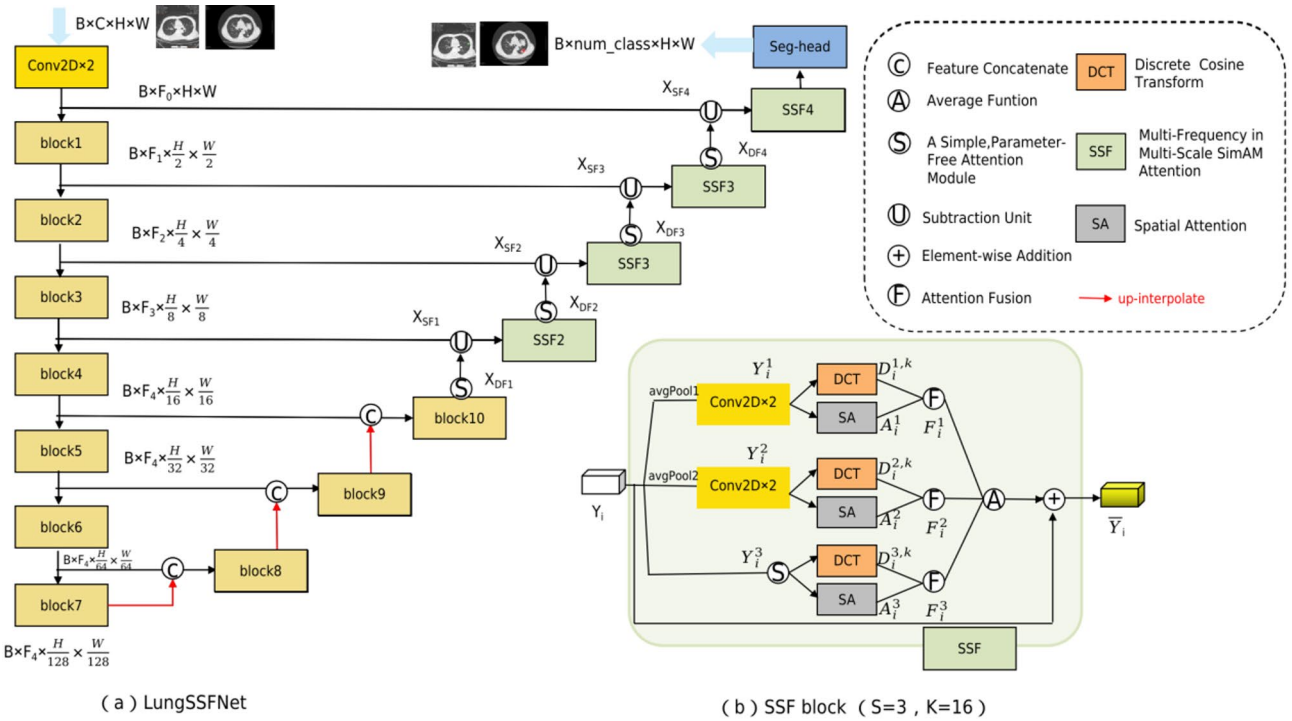

Fig. 1. (**a**) The architecture of LungSSF is constructed with "block" and "SSF" modules. The "block" is composed of two CONV2D layers: the first CONV2D layer has a 3 × 3 kernel with a stride of 1, and the second has a 3 × 3 kernel with a stride of 2. (**b**) First, the "SSF" obtains multi-scale features through pooling with different convolution kernel sizes and SimAM. These multi-scale features are then represented in the spatial domain (Spatial Attention) and the frequency domain (Discrete Cosine Transform). Finally, the characterized multi-scale features are aggregated using the Attention Fusion and Average functions.

the mean squared error loss as the objective function. Additionally, a regularization term is included[29], where λ is the regularization constant, and M = H × W. Subsequently, assuming that there is a uniform distribution of neurons except for the target neuron t, when e_t reaches a minimum value, the corresponding linear function composed of ω_t and b_t is optimal and the target neuron has a higher importance than the other neurons. The mathematical solution of e_t is as follows:

$$e_t^* = \frac{4\left(\sigma_t^2 + \lambda\right)}{(t - \mu_t)^2 + 2\sigma_t^2 + 2\lambda}$$

Finally, this computed weight is multiplied element-wise with the input feature map to obtain the attention weight map, i.e., $SimAM\left(Y_i^s\right)$, as follows:

$$SimAM\left(Y_i^s\right) = \sigma\left(\frac{1}{\mathbf{E}}\right) \odot \mathbf{Y_i^s}$$

To produce multiscale features from the input feature Y_i, pooling layers are used to reduce the dimensionality. For each scale s, the average pooling ($avgPool_s$) kernel size and stride are both set to $2^{(s-1)}$, thus generating Y_i^s only at s = 3, bypassing avgPool and applying SimAM directly. **E** is the result of e after being computed by all neurons.

$$Y_i^s = \text{Conv2D} \times 2\left(\text{avgPool}_s\left(Y_i\right)\right).$$

Consequently, to capture the image in the frequency domain, a previously described method[19] is employed, as follows:

$$D_i^{s,k} = \sum_{h=0}^{H_s-1} \sum_{w=0}^{W_s-1} \left(Y_i^s\right) \mathbf{D}_{h,w}^{u_k,v_k}$$

Moreover, in the manner described previously[30], the 2D discrete cosine transform of the s-th scale branch is defined as follows:

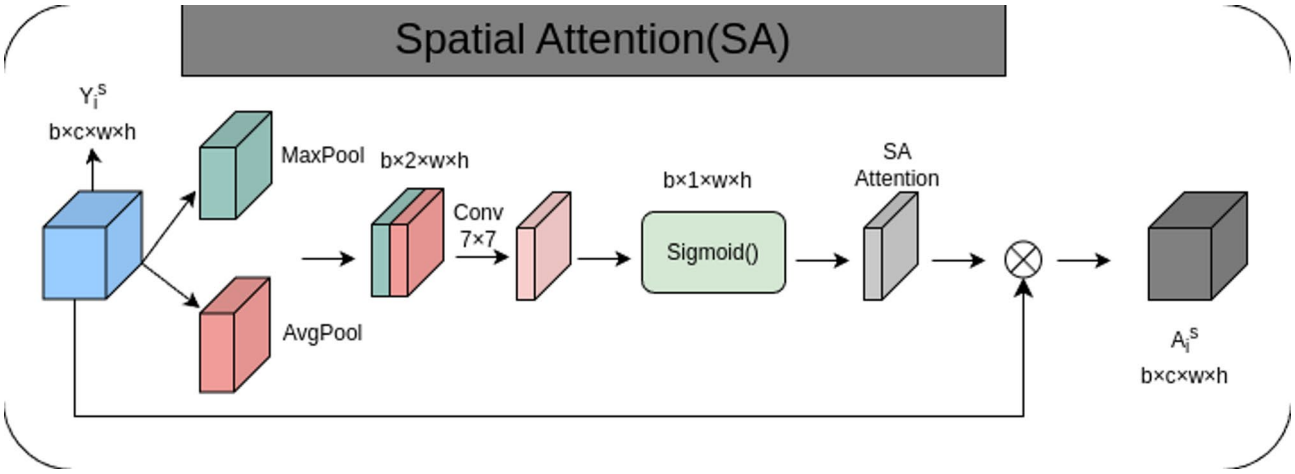

Fig. 2. The spatial attention utilizes two similar outputs that are pooled along the channel axis and forward them to a convolution layer.

	Sample[a]	People[b]
Benign	70	70
Malignant	272	109

Table 1. Details of CT series.

$$D_{h,w}^{u_k,v_k} = \cos\left(\frac{\pi h}{H_s}\left(u_k + \frac{1}{2}\right)\right)\cos\left(\frac{\pi w}{W_s}\left(v_k + \frac{1}{2}\right)\right)$$

where each $D_i^{s,k}$ is transformed into Z_{avg}, Z_{max}, and Z_{min} by global average pooling, global maximum pooling, and global minimum pooling, respectively. Subsequently, the image attention in the space is obtained as follows[31]:

$$A_i^s = SA\left(Y_i^s\right)$$

The following figure illustrates the spatial attention mechanism (Fig. 2).

Next, the feature maps $D_i^{s,k}$ and A_i^s are recalibrated through the frequency domain and spatial domain, and the learnable parameters α_i^s and β_i^s are introduced to control the information between the frequency domain and spatial domain at each different scale, as follows:

$$F_i^s = \mathrm{Conv}\left(\alpha_i^s D_i^{s,k} + \beta_i^s A_i^s\right)$$

Ultimately, F_i^s is reshaped to match Y_i, and F is aggregated at different scales by using the aggregation function A, which is used to check the noise in the image. After aggregation, division by the number of branches and addition with Y_i generates the final output, $\bar{Y}_i$, as follows:

$$\bar{Y}_i = Y_i + \mathbf{A}\left(F_i^s, \mathrm{Up}_s\left(F_i^s\right)\right)$$

Experiments and analysis

Construction of the dataset

Retrospective CT data were collected from patients who underwent radical resection of pulmonary carcinoma and pneumocentesis at Li Huili Hospital, Ningbo Medical Center, and Ningbo No. 1 Hospital in China, spanning from January 2021 to April 2024. Additionally, CT scans from patients diagnosed with pulmonary bulla at Li Huili Hospital from January to December 2023 were gathered and utilized as a control dataset. Descriptive keywords including "vacuole," "cystic cavity," "cystic," and "cavity" were utilized to screen and identify eligible patients. Ultimately, the compiled dataset encompassed 272 CT scans from 109 patients with lung cancer and 70 CT scans from 70 patients with pulmonary bulla, as detailed in Table 1. All data utilized in this study have received formal ethical approval from the Institutional Review Board (IRB) of Ningbo Medical Center Lihuili Hospital, in full compliance with national medical research regulations and international ethical standards.

Inclusion and exclusion criteria

The inclusion criteria for this study were as follows:

1) Preoperative imaging via CT revealing a thin-walled cystic cavity, which may or may not be accompanied by solid or ground-glass nodules.
2) Pathological confirmation of adenocarcinoma in situ, minimally invasive adenocarcinoma, or invasive adenocarcinoma, according to the 9th edition of the tumor, node, and metastasis (TNM) classification system for lung cancer.

The exclusion criteria were as follows:

1) Malignancy confirmed without the aid of surgery or puncture biopsy.
2) CT images that were insufficiently clear to make a definitive diagnosis.
3) Cystic cavities located in the center of previously solid lesions, suggesting the possibility of cavitation.
4) Cystic cavities that could not be reliably differentiated from surrounding emphysema, bronchiectasis, or pulmonary pemphigoid.

Data extraction

The chest CT series were acquired utilizing the Brilliance CT 16 Slice and Toshiba Aquilion 64 CT systems. We used this machine to scan the patient's lungs, with the voltage fixed at 120 kVP. These series featured a layer thickness of less than 1.5 mm and were captured with a matrix resolution varying between 512 mm × 512 mm, 1024 mm × 1024 mm, 1445 mm × 927 mm, and 1284 mm × 594 mm. Subsequently, the chest CT series were converted into the .nii format and imported into the Pair V 2.8 software (available at aipair.com.cn) for the purpose of marking and analysis.

Experimental details

For all training and experiments, we used a 13th -generation Intel® Core™ 16-core i7-13700 K CPU running an Ubuntu 20.04.6 operating system, together with an RTX4090 GPU, 24 GB of RAM, 62 GiBson of RAM, and a PyTorch 2.2.2 deep learning framework. In the training phase, a stochastic gradient descent optimizer with Nesterov momentum and an initial learning rate of 0.01, a weight decay of 3e-5, and a momentum of 0.99 was used. This optimizer was combined with a polynomial-decay learning rate scheduler to adjust the learning rate during training. Considering the memory capacity of the GPU, the batch size was set to 7 in experiments. To ensure model convergence, all experimental networks were trained for 500 epochs. In addition, binary cross-entropy loss and a soft Dice loss function (a well-known loss function in medical image segmentation) were used to optimize the training process of LungSSFNet.

Design of experiments

To demonstrate the effectiveness of LungSSFNet, six network experiments were conducted separately using (1) UNet, (2) M^2SNet, (3) TANet, (4) MADGNet, (5) nnUNet, and (6) LungSSFNet.

Evaluation of indicators

The Dice similarity coefficient (DSC) and the intersection over union (IoU) were used to assess the results of automatic segregation of test sets. Accuracy, precision, and sensitivity (i.e., recall) were used to evaluate the applicability of models. In addition, F1_scores were calculated to evaluate the performance of the models.

Results

Construction of LungSSFNet

First, we adopted nnUNet as the basic network architecture and named it "Lung". Subsequently, we tested attention mechanisms, which named CBAM and SimAM. The results (Table 2) showed that LungSimAM performed slightly better than LungCBAM. Thus, we used the SSF block with the LungSimAM network architecture to obtain LungSSF1. However, the addition of multi-frequency resulted in a significant decrease in model performance. We considered that this might have been due to the inefficient application of computational resources in the traditional U-Net architecture to shallow features that provide few image features. Another possible explanation is that the introduction of multi-frequency features has increased the complexity of the

Model	Label	IoU	DSC
LungCBAM	Malignant	78.42	71.79
	Benign	92.61	91.13
LungSimAM	Malignant	79.72	72.99
	Benign	92.73	91.56
LungSSF1	Malignant	71.48	66.66
	Benign	90.14	89.13
LungSSF2	Malignant	78.99	72.12
	Benign	93.00	91.97
LungSSFNet	Malignant	81.05	75.15
	Benign	93.03	92.04

Table 2. Ablation experiments of different attention mechanisms in the same framework.

model, leading to overfitting or difficulties in optimizing the training process. Moreover, Cao et al.[32] proposed that, in comparison to shallow features, deeper semantic features extracted from deeper convolutional layers contain more informative content. Guided by this principle and through rigorous ablation experiments, we ultimately arrived at the LungSSFNet architecture. In LungSSF2, the SSF module consisted of four blocks, and in LungSSF1, the SSF module consisted of seven blocks. Our findings revealed that an increase in the number of SSF blocks led to a decline in model performance. Consequently, through additional ablation studies, we conclusively determined that four SSF blocks represented the optimal configuration.

Segmentation ability of LungSSFNet

Subsequently, we randomly grouped 342 CT series into a training set, consisting of 245 series manually annotated by thoracic surgeons, to train the LungSSFNet model. In addition, 62 series were used as a validation set to be labeled by thoracic surgeons and by LungSSFNet to validate and coordinate LungSSFNet. Finally, 35 series form the test set were used to evaluate the validity and accuracy of LungSSFNet. As shown in Fig. 3, LungSSNet had higher accuracy than the classical model for cases of tumors and of pulmonary bullae. In addition, as shown in Fig. 4, the area segmented by LungSSNet was largely where cystic-cavity lesions were located.

As illustrated in Fig. 5, our model occasionally misclassifies individual malignant images as green (normal). This may stem from the notably higher proportion of solid components in these cystic cavities compared to air-containing ones, highlighting a current limitation in our model's architecture. However, with the continuous integration of additional experimental data, the model is expected to significantly reduce the likelihood of false negatives.

Table 3 illustrates that LungSSFNet exhibited superior segmentation performance compared to other models. For example, compared with nnUNet, the existing optimal model, LungSSFNet achieved a DSC and IoU that were 1.61% and 1.14% higher, respectively, for tumor areas, and 0.74% and 0.42% higher, respectively, for benign areas. This underscores that LungSSFNet surpasses nnUNet in terms of graphical segmentation accuracy. Furthermore, compared with MADGNet, which is also multi-scale and multi-frequency, LungSSFNet had a DSC and IoU that were 0.96% and 1.38% higher, respectively.

Results of multiple comparative experiments

Table 4 presents the results of comparative experiments conducted with models that shared identical training parameters. Once again, LungSSFNet demonstrated superior performance across all evaluated metrics compared to the other models. Specifically, when compared to nnUNet, LungSSFNet exhibited a 2.84% increase in accuracy, a 3.85% enhancement in precision, and a 1.88% higher F1-score.

Discussion

Most LCCAs have an insidious onset, and patients with LCCAs do not have obvious clinical symptoms. Low-dose CT is one of the most suitable screening tools for LCCA. However, management guidelines related to lung nodules have not yet proposed appropriate diagnostic criteria specifically for LCCA, less to say for early-stage

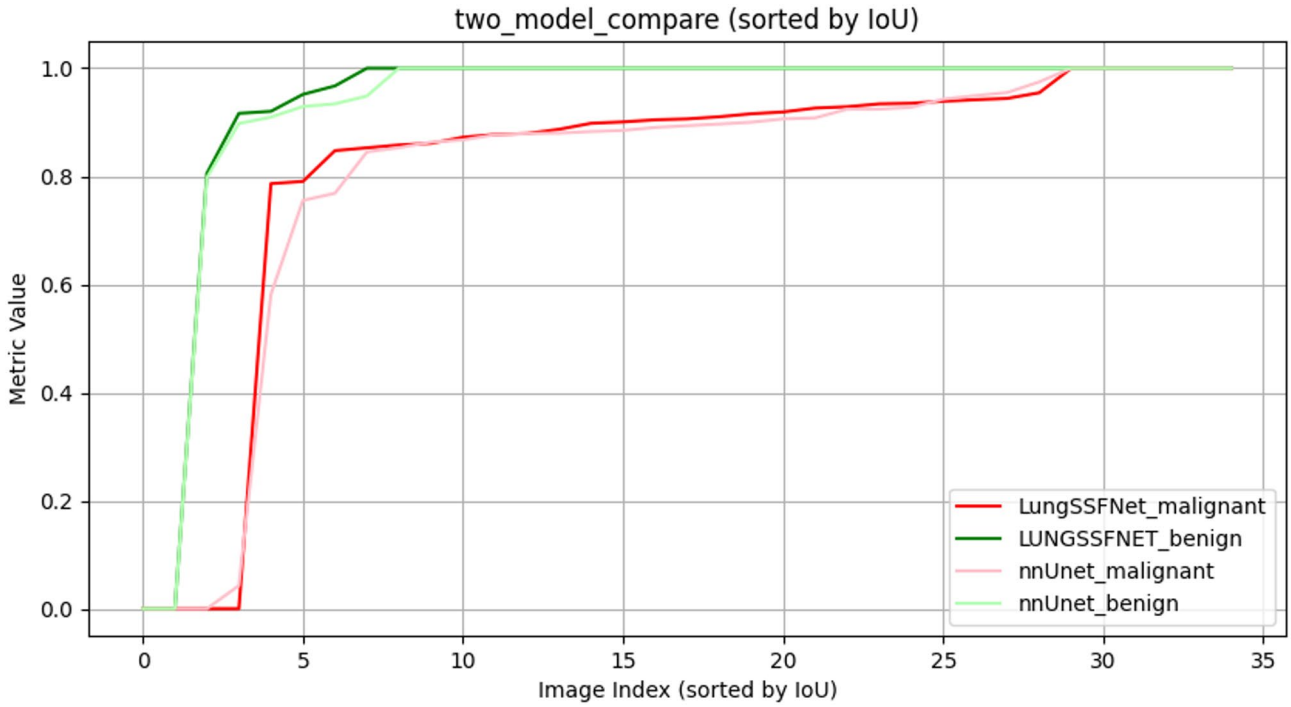

Fig. 3. nnUNet and LungSSFNet compare on 35 test cases.

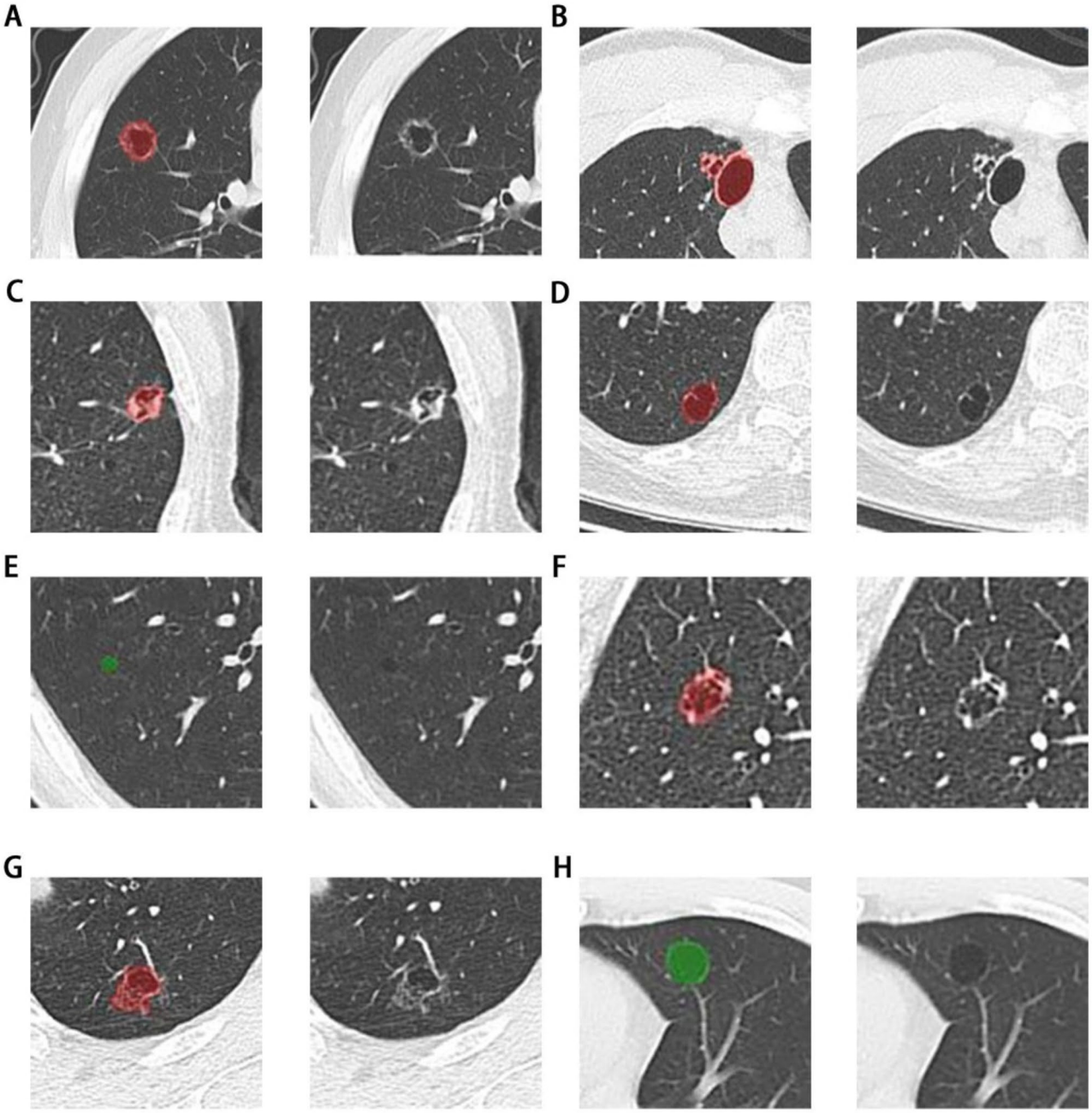

Fig. 4. LungSSFNet segmentation results: A-G (malignant, red) vs. H (benign, green). Left: annotated image with color-coded regions; Right: original unannotated image.

LCCA[37]. A general classification system was created by Shen et al.[13]: type I for thin-walled cysts (< 2 mm), type II for thick-walled cysts (≥ 2 mm), type III for lesions with endophytic or ectophytic nodules, and type IV for multicystic lesions with a mixture of solid or non-solid components. The morphology of the outer wall or the nodularity of cystic-cavity lesions is one of the key characteristics that identifies these lesions as benign or malignant. Therefore, rapid and accurate identification and effective segmentation of cystic-cavitary lesions in chest CT images is a key step in clinical decision-making. Consequently, efficient segmentation is essential for the early diagnosis of LCCA and determination of a treatment plan to improve the prognosis and reduce the mortality rates of patients.

Due to the lack of effective tools for reading CT images, the early underdiagnosis rate of LCCA is as high as 22.7%[14]. Therefore, combining multi-convolutional arithmetic technology with the deep learning functionality of AI could provide a new and practical method for the diagnosis of LCCA that may be applicable to the development of diagnostic and treatment protocols for this disease. Furthermore, unlike traditional machine learning, deep learning has powerful feature-extraction capabilities[38]. Specifically, deep learning does not rely on manually designed features; rather, it captures subtle information embedded in images to understand

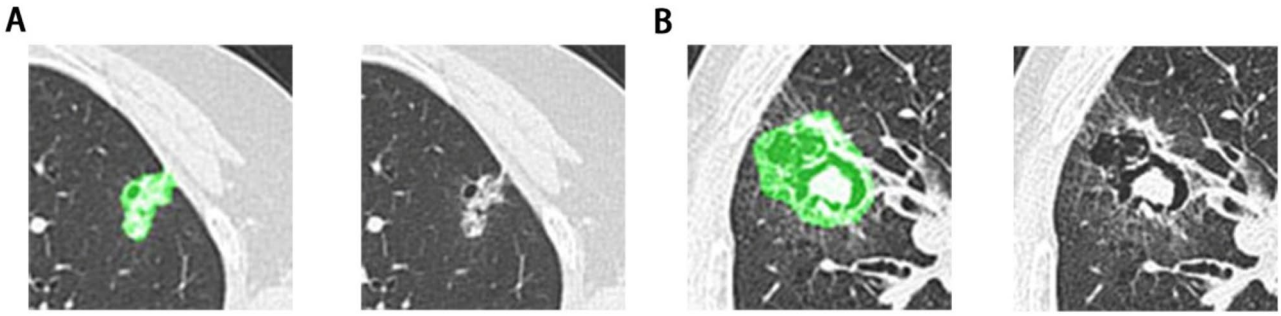

Fig. 5. Bad segmentations: A-B(malignant, green). Left: annotated image with color-coded regions; Right: original unannotated image.

Model	Label	IoU	DSC
UNet[33]	Malignant	76.04	70.59
	Benign	89.62	88.23
M^2SNet[34]	Malignant	69.69	62.15
	Benign	84.34	83.23
TANet[35]	Malignant	74.63	68.68
	Benign	89.83	88.57
MADGNet[19]	Malignant	79.67	74.19
	Benign	90.25	89.33
nnUNet[36]	Malignant	79.91	73.54
	Benign	92.61	91.30
LungSSFNet	Malignant	81.05	75.15
	Benign	93.03	92.04

Table 3. Segmentation results in model performance.

Model	Accuracy	Precision	Sensitivity	F1_Score
UNet	93.93	96.15	96.15	96.15
M^2SNet	93.93	100.00	92.85	96.29
TANet	90.90	92.30	96.00	94.11
MADGNet	93.75	96.15	96.15	96.15
nnUNet	93.93	96.15	96.15	96.15
LungSSFNet	96.77	100.00	96.15	98.03

Table 4. Recognition effect of different models.

the different features of lesions at margins, at different resolutions and scales from a multiscale perspective[39]. Deep learning can also optimize the processing pattern of an image using convolutional kernels and variable dimensional pooling layers to facilitate image segmentation. Furthermore, deep learning can perform high-throughput sequencing of clinical samples, and processing with deep learning and modeling can proceed to genome-wide association studies[40,41]. Such studies can reveal epigenetic patterns and predict the growth trend of cystic cavities and provide substantial references for the prevention and diagnosis of LCCA.

In this study, we introduced a model named LungSSFNet, which identifies and diagnoses LCCA by analyzing chest CT series. In terms of segmentation performance, LungSSFNet achieved a DSC accuracy of 75.15 for LCCA, surpassing existing models by a margin of 1–13%. This outcome suggests that LungSSFNet is capable of restoring edge details in segmentation results more accurately than other models, thereby facilitating the extraction of image features (as shown in Table 4). When it comes to specificity and accuracy, LungSSFNet exhibited superior performance compared to the tested models. However, in terms of sensitivity, its performance was comparable to that of the existing models. Moving forward, we aim to further enhance the performance of LungSSFNet. One potential approach could involve utilizing a vast number of annotated datasets to train the model, enabling it to generalize across various cystic lung diseases and improve its differential diagnostic capabilities.

While LungSSFNet represents a significant breakthrough, our study was constrained by the use of a small, single-center dataset. Therefore, it is imperative that we gather extensive clinical data, particularly from multiple

centers, and consistently train LungSSFNet on this expanded dataset to enhance its precision and accuracy in segmenting CT images.

In conclusion, we have developed LungSSFNet, a task-specific deep learning framework optimized for pulmonary CT image segmentation, which exhibits high translational potential in clinical practice. By integrating multi-scale contextual feature extraction with boundary-aware refinement, the model achieves robust segmentation performance across heterogeneous CT datasets, particularly in identifying early-stage or ambiguous lesions associated with lung cancer. These capabilities suggest LungSSFNet's potential as a clinically viable tool for radiologists, facilitating objective, quantitative lesion assessments to support diagnostic decision-making in LCCA screening and staging.

Data availability

The datasets generated and analyzed during the current study are not publicly available due to protection of individual patient privacy but are available from the corresponding author on reasonable request.

Received: 17 January 2025; Accepted: 5 June 2025
Published online: 02 July 2025

References

1. BRAY, F. & LAVERSANNE, M. Global cancer statistics 2022: GLOBOCAN estimates of incidence and mortality worldwide for 36 cancers in 185 countries [J]. *Cancer J. Clin.* **74** (3), 229–263 (2024).
2. SIEGEL, R. L. et al. Cancer statistics, 2023 [J]. *Cancer J. Clin.* **73** (1), 17–48 (2023).
3. HENDRIKS, L. et al. Non-small-cell lung cancer. *J* **10** (1), 71 (2024).
4. MAZZONE, P. J. Evaluating the patient with a pulmonary nodule: A review [J]. *Jama* **327** (3), 264–273 (2022).
5. SNOECKX, A. & REYNTIENS, P. Diagnostic and clinical features of lung cancer associated with cystic airspaces [J]. *J. Thorac. Disease*. **11** (3), 987–1004 (2019).
6. GUO, J. et al. [Thin-walled cystic lung cancer: an analysis of 24 cases and review of literatures] [J]. Zhongguo Fei Ai Za zhi = chinese. *J. Lung cancer*. **17** (7), 553–556 (2014).
7. MARIO, M. et al. *Lung cancer Assoc. Cyst. Airspaces [J] Comput Assist Tomogr 2015 Jan-Feb;39(1):102-8* **39**(1) (2014).
8. ANDERSON H J, PIERCE, J. W. Carcinoma of the bronchus presenting as thin-walled cysts [J]. *Thorax* **9** (2), 100–105 (1954).
9. RUPNIK E J, P. E. A. B. O. D. Y. J. W. J. R. & HANNER, J. M. Bronchial carcinoma masquerading as a thin-walled cyst [J]. The American journal of roentgenology, radium therapy, and nuclear medicine, 77(6): 1051-4. (1957).
10. GOLDSTEIN, M. J. et al. Bronchogenic carcinoma and giant bullous disease [J]. *Am. Rev. Respir. Dis.* **97** (6), 1062–1070 (1968).
11. HURLEY, P. & CORBISHLEY, C. Bronchioloalveolar carcinoma arising in longstanding lung cysts [J]. *Thorax* **40** (12), 960 (1985).
12. ARONBERG D J, SAGEL S S, L. E. F. R. A. K. S. et al. Lung carcinoma associated with bullous lung disease in young men [J]. *AJR Am. J. Roentgenol.* **134** (2), 249–252 (1980).
13. SHEN, Y. et al. Lung cancers associated with cystic airspaces: CT features and pathologic correlation [J]. *Lung cancer (Amsterdam Netherlands)*. **135**, 110–115 (2019).
14. SCHOLTEN E T et al. Computed tomographic characteristics of interval and post screen carcinomas in lung cancer screening [J]. *Eur. Radiol.* **25** (1), 81–88 (2015).
15. SHEARD, S. et al. *Lung Cancers Associated with Cystic Airspaces: Underrecognized Features of Early Disease [J]*38704–717 (a review publication of the Radiological Society of North America, Inc, 2018). 3.
16. BHINDER, B. et al. Artificial intelligence in Cancer research and precision medicine [J]. *Cancer Discov.* **11** (4), 900–915 (2021).
17. SHIMIZU, H. NAKAYAMA K I. Artificial intelligence in oncology [J]. *Cancer Sci.* **111** (5), 1452–1460 (2020).
18. PRABHU, S. et al. AI-based carcinoma detection and classification using histopathological images: A systematic review [J]. *Comput. Biol. Med.* **142**, 105209 (2022).
19. JU-HYEON NAM N S S, SU JUNG KIM, SANG-CHUL, L. E. E. *Modality-agnostic Domain Generalizable Medical Image Segmentation by Multi-Frequency in Multi-Scale Attention [J]* (Electrical Engineering and Systems Science, 2024).
20. RIKHARI, H. et al. Improving lung nodule segmentation in thoracic CT scans through the ensemble of 3D U-Net models [J]. *Int. J. Comput. Assist. Radiol. Surg.* **19** (10), 2089–2099 (2024).
21. YEUNG, M. & SCHöNLIEB, S. A. L. A. E. Focus U-Net: A novel dual attention-gated CNN for polyp segmentation during colonoscopy [J]. *Comput. Biol. Med.* **137**, 104815 (2021).
22. MONKAM, P. et al. Detection and classification of pulmonary nodules using convolutional neural networks: A survey [J]. *IEEE Access.* **7**, 78075–78091 (2019).
23. LI, R. et al. Deep learning applications in computed tomography images for pulmonary nodule detection and diagnosis: A review [J]. *Diagnostics (Basel).* **12**(2), 298 (2022).
24. SUN, J. et al. Deep learning-based solid component measuring enabled interpretable prediction of tumor invasiveness for lung adenocarcinoma [J]. *Lung Cancer.* 186, 107392 (2023).
25. CARDENAS C et al. Deep learning algorithm for Auto-Delineation of High-Risk oropharyngeal clinical target volumes with Built-In dice similarity coefficient parameter optimization function [J]. *Int. J. Radiat. Oncol. Biol. Phys.* **101** (2), 468–478 (2018).
26. MEN, K., DAI, J. & LI, Y. Automatic segmentation of the clinical target volume and organs at risk in the planning CT for rectal cancer using deep dilated convolutional neural networks [J]. *Med. Phys.* **44** (12), 6377–6389 (2017).
27. WANG, C. & TYAGI, N. RIMNER A, et al. Segmenting lung tumors on longitudinal imaging studies via a patient-specific adaptive convolutional neural network [J]. *Radiotherapy oncology: J. Eur. Soc. Therapeutic Radiol. Oncol.*, **131**: 101–107. (2019).
28. GUO, Z. et al. Gross tumor volume segmentation for head and neck cancer radiotherapy using deep dense multi-modality network [J]. *Phys. Med. Biol.* **64** (20), 205015 (2019).
29. NAIK, A. & EDLA D R J W P C. Lung Nodule Classification on Computed Tomography Images Using Deep Learning [J]. (12). (2020).
30. LI, Z Q A P Z A F W A & X. FcaNet: Frequency Channel Attention Networks [J]. Computer Science, (2012).
31. HETTIHEWA, K. et al. MANet: a multi-attention network for automatic liver tumor segmentation in computed tomography (CT) imaging [J]. *Sci. Rep.* **13** (1), 20098 (2023).
32. CAO, K. et al. Large-scale pancreatic cancer detection via non-contrast CT and deep learning [J]. *Nat. Med.* **29** (12), 3033–3043 (2023).
33. RONNEBERGER, O., FISCHER, P. & U-Net, B. R. O. X. T. *Convolutional Networks for Biomedical Image Segmentation* (Springer International Publishing, 2015). [C].
34. SCHLEMPER, J. & OKTAY, O. Attention gated networks: learning to leverage salient regions in medical images [J]. *Med. Image. Anal.* **53**, 197–207 (2019).
35. LI, Y. et al. TA-Net: triple attention network for medical image segmentation [J]. *Comput. Biol. Med.* **137**, 104836 (2021).

36. ISENSEE, F. et al. nnU-Net: a self-configuring method for deep learning-based biomedical image segmentation [J]. *Nat. Methods.* **18** (2), 203–211 (2021).
37. MACMAHON, H. et al. Guidelines for management of incidental pulmonary nodules detected on CT images: from the Fleischner society 2017 [J]. *Radiology* **284** (1), 228–243 (2017).
38. AGNES, S. A. Appraisal of Deep-Learning techniques on Computer-Aided lung Cancer diagnosis with computed tomography screening [J]. *J. Med. Phys.* **45** (2), 98–106 (2020).
39. QUANYANG, W. et al. Artificial intelligence in lung cancer screening: detection, classification, prediction, and prognosis [J]. *Cancer Med.* **13** (7), e7140 (2024).
40. ABDELLAOUI, A. et al. 15 years of GWAS discovery: realizing the promise [J]. *Am. J. Hum. Genet.* **110** (2), 179–194 (2023).
41. PERROTT S L & KAR S P. Polygenic risk scores for genomics and population screening [J]. *Lancet (London England).* **404** (10456), 935–936 (2024).

Author contributions
Zeyang Hu: Methodology, Formal analysis, Writing - original draft, Writing - review & editing. Guodong Xu, Wei Shen, Bailing Zhang: Methodology, Formal analysis, Writing - review & editing. Xia Zhang, Chaoyi Pang, Jian Tan, Jinqiu Yang and Yipeng Zhou : Software, Hang Chen, Hongxiang LI, Jiaheng Zhang, Keyue Qiu and Zijun Xie: Data curation.

Funding information
This work was partially supported by the Key R&D projects of Zhejiang Province [2024C03277(SD2)], Ningbo Youth Science and Technology Innovation Leading Talents Program [grant number 2023QL055] and Key Clinical Specialty Construction Project of Zhejiang Province.

Declarations

Competing interests
The authors declare no competing interests.

Conflict of interest
The authors report no declarations of interest. Each participant agrees to the publication of this article.

Human ethics and consent to participate declarations
Not applicable. For this study informed consent has been waived by the IRB of Ningbo Medical Center Lihuili Hospital(KY2024SL343-01) due to the anonymity and retrospective nature of the study.

Additional information
Correspondence and requests for materials should be addressed to G.X., J.T. or C.P.